accepted manuscript at https://doi.org/10.1016/j.cmpb.2024.108271

# Highlights

**Effect of variability of mechanical properties on the predictive capabilities of vulnerable coronary plaques**

Marco Stefanati, Anna Corti, Valentina Corino, Martin R Bennett, Zhongzhao Teng, Gabriele Dubini, José Félix Rodriguez Matas

- Biomechanical markers based on the peak plaque structural stress outperform classifiers based on plaque geometric features only when uncertainty in the mechanical properties of plaque components is accounted for.
- Peak plaque structural stress calculated based on linear elastic material models provides a good marker for plaque vulnerability classification outperforming non linear models.
- Classifiers of plaque vulnerability based on peak plaque structural stress in combination with patients' arterial pressure may improve the classification power.

accepted manuscript at https://doi.org/10.1016/j.cmpb.2024.108271

# Effect of variability of mechanical properties on the predictive capabilities of vulnerable coronary plaques

Marco Stefanati[a,*], Anna Corti[b], Valentina Corino[b], Martin R Bennett[c], Zhongzhao Teng[c,d,e], Gabriele Dubini[a], José Félix Rodriguez Matas[a]

[a]*Department of Chemistry, Materials and Chemical Engineering "Giulio Natta", Politecnico di Milano, Piazza Leonardo da Vinci 32, Milan, 20133, Italy*
[b]*Department of Electronics, Informatics and Bioengineering, Politecnico di Milano, Via Ponzio 34/5, Milan, 20133, Italy*
[c]*Division of Cardiovascular Medicine, University of Cambridge, Addenbrookes Hospital, Hills Road, Cambridge, CB2 0QQ, United Kingdom*
[d]*Department of Radiology, University of Cambridge, School of Clinical Medicine, Box 218, Level 5, Hills Road, Cambridge, CB2 0QQ, United Kingdom*
[e]*Nanjing Jingsan Medical Science and Techonology, Ltd., 6# Shuiyougang Rd., Gulou, Nanjing, Jiangsu, China*

## Abstract

*Background and Objective:* Coronary plaque rupture is a precipitating event responsible for two thirds of myocardial infarctions. Currently, the risk of plaque rupture is computed based on demographic, clinical, and image-based adverse features. However, using these features the absolute event rate per single higher-risk lesion remains low. This work studies the power of a novel framework based on biomechanical markers accounting for material uncertainty to stratify vulnerable and non-vulnerable coronary plaques.
*Methods:* Virtual histology intravascular ultrasounds from 55 patients, 29 affected by acute coronary syndrome and 26 affected by stable angina pectoris, were included in this study. Two-dimensional vessel cross-sections for finite element modeling (10 sections per plaque) incorporating plaque structure (medial tissue, loose matrix, lipid core and calcification) were reconstructed. A Montecarlo finite element analysis was performed on each section to account for material variability on three biomechanical markers: peak plaque structural stress at diastolic and systolic pressure, and peak plaque stress

*Corresponding author, e-mail: marco.stefanati@polimi.it, address: Piazza Leonardo da Vinci 32, Milan, 20133, Italy

difference between systolic and diastolic pressures, together with the luminal pressure. Machine learning decision tree classifiers were trained on 75% of the dataset and tested on the remaining 25% with a combination of feature selection techniques. Performance against classification trees based on geometric markers (i.e., luminal, external elastic membrane and plaque areas) was also performed.
*Results:* Our results indicate that the plaque structural stress outperforms the classification capacity of the combined geometric markers only (0.82 vs 0.51 area under curve) when accounting for uncertainty in material parameters. Furthermore, the results suggest that the combination of the peak plaque structural stress at diastolic and systolic pressures with the maximum plaque structural stress difference between systolic and diastolic pressures together with the systolic pressure and the diastolic to systolic pressure gradient is a robust classifier for coronary plaques when the intrinsic variability in material parameters is considered (area under curve equal to [0.91 - 0.93]).
*Conclusion:* In summary, our results emphasize that peak plaque structural stress in combination with the patient's luminal pressure is a potential classifier of plaque vulnerability as it independently considers stress in all directions and incorporates total geometric and compositional features of atherosclerotic plaques.

*Keywords:* Coronary artery, atherosclerosis, finite element method, plaque structural stress

## 1. Introduction

Coronary plaque rupture is the precipitating event in two-thirds of myocardial infarctions [1]. Precursors lesions for rupture include a thin overlying fibrous cap that separates the core from the lumen, identified as a thin-cap fibroatheroma (TCFA) [2], and the presence of a large, necrotic lipid core [3]. However, in vivo imaging modalities for coronary atherosclerosis have historically lacked sufficient resolution to accurately and reproducibly identify plaque composition and architecture. Virtual histology intravascular ultrasound (VH-IVUS), an invasive, ultrasound-based modality, uses backscatter to distinguish plaque components such as dense calcium, fibrofatty tissue, fibrous tissue, and necrotic core [4, 5]. Prospective studies utilizing VH-IVUS-defined plaque classification algorithms have demonstrated an association be-

tween VH-IVUS-defined TCFA and subsequent major adverse cardiovascular events [6, 7]; however, the absolute event rate per individual higher-risk lesion was low. Therefore, additional methods to assess plaque vulnerability are required to enhance our ability to predict plaque rupture.

Nowadays, there is a pressing need for novel diagnostic screening methods to identify vulnerable plaques before rupture, aiming to determine the most appropriate intervention or treatment for the patient. This is crucial because certain features alone do not consistently identify vulnerable plaques. Increased plaque structural stress (PSS) is a potential mechanism that promotes plaque rupture, occurring when PSS exceeds the mechanical strength [8]. In fact, Finite Element Methods (FEM) constructed using ex vivo data from histology have shown that ruptured plaques are linked to higher PSS levels, increased necrotic core size, decreased fibrous cap thickness, and micro-calcification [9, 10, 11, 12].

In this study, we introduce a methodology utilizing FEM to compute PSS and evaluate the vulnerability of atherosclerotic plaques in patient-specific coronary arteries based on in vivo VH-IVUS data from 55 patients. Of these, 29 had unstable angina pectoris (G1 group) and 26 had chronic stable angina (G2 group). The VH-IVUS data were processed to reconstruct vessel geometry and plaque architecture, enabling the construction of two-dimensional (2D) vessel cross-sections for FEM modeling. The FEM model allows biomechanical simulation of the complete cardiac cycle (diastole and systole) in the selected 2D coronary sections. It analyzes Von Mises stress along the coronary tract, establishing specific thresholds for both patient groups to identify a risk classifier. This classifier estimates the probability of atherosclerotic plaque rupture and designs representative models, considering specific patient characteristics for optimal intervention and treatment planning.

To assess the classification ability of PSS, various material formulations for plaque components were considered, including linear and non-linear materials. The intrinsic variability of their mechanical properties was incorporated in simulations via Monte Carlo simulation.

## 2. Methods

### *2.1. Procedural Details*

The research protocols for the Vulnerable Atherosclerosis (VIVA) study involving VH-IVUS were approved by the Cambridge Research Ethics Committee [6]. In brief, the study involved 170 patients who underwent VH-IVUS

for three coronary vessels, 100 with stable angina pectoris (SAP) and 70 with troponin-positive acute coronary syndrome (ACS). Among these participants, 61 individuals were included, with 35 categorized as having "unstable plaque" (i.e. ACS, G1 group) and 26 as having "stable plaque" (i.e. SAP, G2 group). For additional details regarding image acquisition, plaque definition and clinical plaque classification we refer to a previous study [13]. The study collected diastolic and systolic pressure data from simultaneous coronary pressure recordings during VH-IVUS acquisition. To mitigate bias arising from differences in arterial pressure, we considered patients who exhibited no significant differences in diastolic pressure (averaging 9.50 kPa for G1 and 9.23 kPa for G2 group, p-value=0.49), systolic pressure (averaging 18.07 kPa for G1 and 16.73 kPa for G2 group, p-value=0.056), and dynamic pressure, defined as the difference between systolic and diastolic pressures, (averaging 8.57 kPa for G1 and 7.50 kPa for G2 group, p-value=0.058). Therefore, 29 patients from the G1 group and 26 patients from the G2 group were selected.

A plaque was defined when plaque burden (PB) was >40% of vessel cross-sectional area for 3 consecutive frames. Both gray-scale (GS) and VH-IVUS-defined IVUS parameters were calculated along each artery, including PB, luminal area (LA), and VH-IVUS-defined plaque composition.

### *2.2. FEM Modeling*

Utilizing radiofrequency data collected at each R-wave peak in vivo, an in-house MATLAB software (The MathWorks Inc) was used for the reconstruction of vessel shape and plaque structure, allowing the creation of 2-dimensional (2D) vessel cross-sections for FEM modeling [13]. Since the data were acquired during diastole, the vessel circumference was reduced, establishing a zero-pressure condition as a basis for computational simulation [14]. In particular, to obtain the zero-pressure geometry, slices of the vessel were shrunk non-uniformly using an iterative approach until the pressurized lumen contour and fibrous cap thickness had the best match with the in-vivo image (obtained under diastolic pressure). So, when the diastolic pressure was applied, the vessel recovered its in vivo-geometry. Figure 1 shows the in-vivo under diastolic pressure and zero-pressure geometries (Fig. 1b) with the von MISES stress under diastolic pressure, $\text{MISES}^{dia}$ (Fig. 1c), and systolic pressure, $\text{MISES}^{sys}$ (Fig. 1d). Approximately 10 sections, evenly distributed along the coronary segment, were analysed for each patient. Given that each plaque encompassed multiple VH-IVUS slices, a linear mixed model was employed to compare plaques between patients and clinical presentations. Fig-

ure 2 depicts the dynamic von MISES stress ($MISES^{dyn}$) fields of coronary vessel sections containing different tissue compositions. Modeling focused on segmenting four components of the atherosclerotic plaque: medial tissue, loose matrix, lipid core, and calcifications, following the procedure detailed elsewhere [13]. Figure 3a illustrates a representative cross-section exhibiting the four plaque components, along with a detailed view of the FEM mesh (Fig. 3b) used for the numerical simulation.

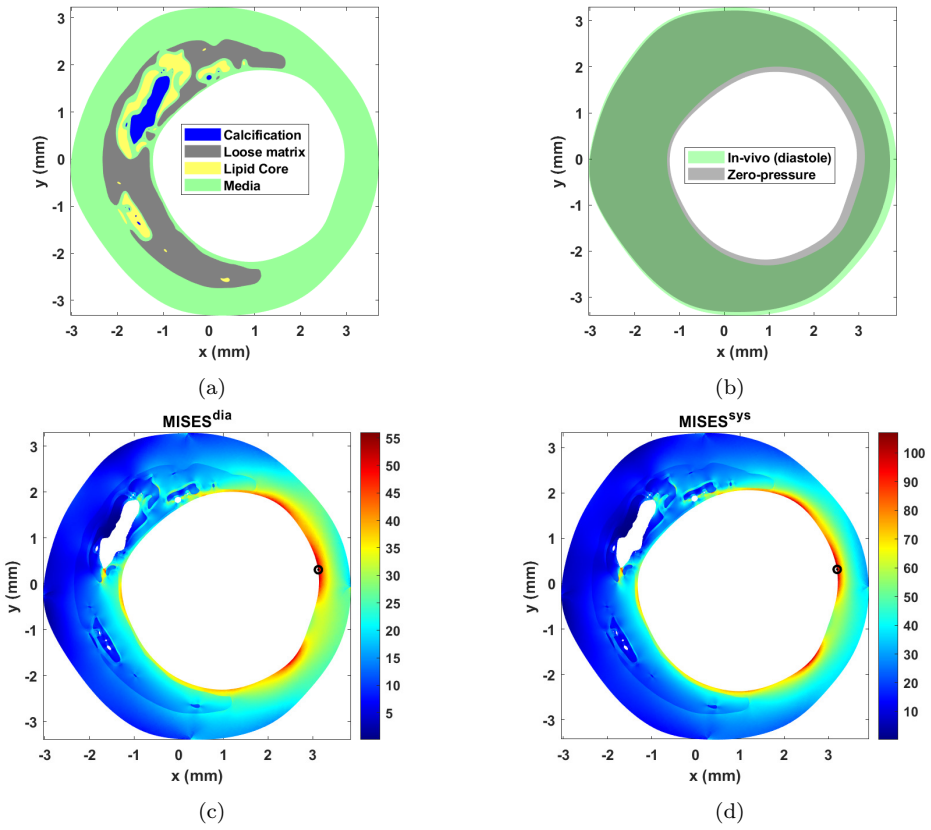


Figure 1: (a) Tissue composition of a coronary vessel section; (b) in-vivo under diastolic pressure and zero-pressure geometries; (c) von MISES stress under diastolic pressure, $MISES^{dia}$; and (d) von MISES stress under systolic pressure, $MISES^{sys}$. A black circle indicates the maximum of von MISES stress.

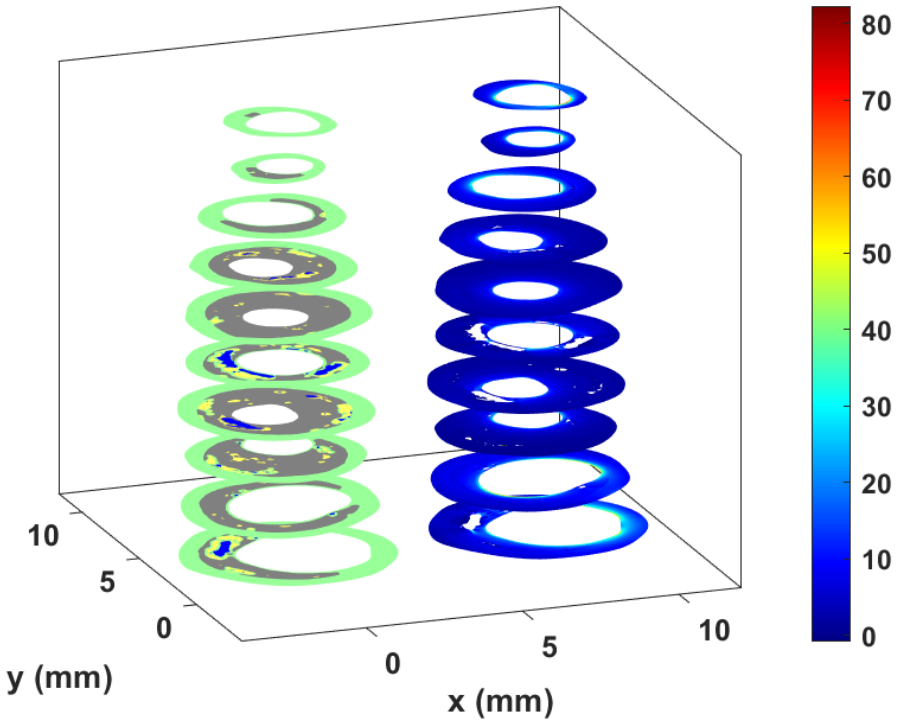


Figure 2: Dynamic von MISES stress ($\text{MISES}^{dyn}$) fields of coronary vessel sections containing different tissue compositions. Calcification is shown in blue, loose matrix in grey, lipid core in yellow and media tissue in green.

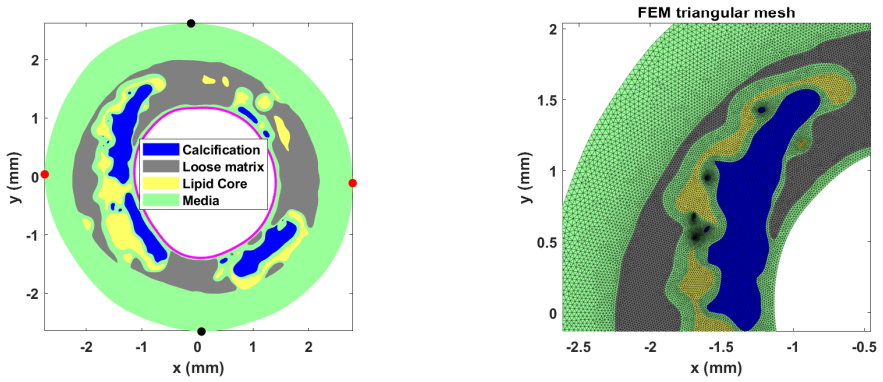


(a) (b)

Figure 3: Typical FEM modeling of a coronary section: (a) Vessel geometry and plaque architecture; and (b) Vessel cross-section for FEM modeling. The red/black points indicate where one dimension displacements are fixed (Dirichlet conditions), while the magenta curve indicates where the pressure is applied (Neumann condition).

Apart from accounting for the intrinsic variability inherent in biological tissues, another crucial decision pertains to the material formulation used for simulation when conducting finite element analysis of atherosclerotic plaques [15, 16]. To explore the influence of material formulation and variability in mechanical properties, four sets of simulations were performed for each analysed plaque section: (i) Components considered as nonlinear elastic with variable mechanical properties, designated as Hyper Variable (HV) simulations; (ii) Components treated as nonlinear elastic with average mechanical properties, labeled as Hyper Mean (HM) simulations; (iii) Components regarded as linear elastic with variable mechanical properties, termed as Linear Variable (LV) simulations; and (iv) Components seen as linear elastic with average mechanical properties, identified as Linear Mean (LM) simulations. Calcifications were presumed to be linear isotropic in all simulations, maintaining either variable or average properties depending on the particular case under consideration [17].

The different components of the plaque and the media were modelled as quasi incompressible hyper-elastic materials, assuming a Poisson's ratio, $\nu$=0.475, with the exception of calcifications for which $\nu$=0.3 was used. For the case of the nonlinear elastic behavior, the media, loose matrix, and lipid core were described by the Yeoh strain energy density function:

$$W\left(\bar{\mathbf{C}}\right) = C_{10}\left(\bar{I}_1 - 3\right) + C_{20}\left(\bar{I}_1 - 3\right)^2 + C_{30}\left(\bar{I}_1 - 3\right)^3 + K\left(J - 1\right)^2, \quad (1)$$

where $\bar{\mathbf{C}} = J^{-2/3}\mathbf{C}$ is the modified right Cauchy-Green deformation tensor, $\mathbf{C} = \mathbf{F}^T\mathbf{F}$ is the right Cauchy-Green deformation tensor, $\mathbf{F}$ the deformation gradient, $J = \det \mathbf{F}$ is the Jacobian, $\bar{I}_1 = \mathrm{tr}\left(\bar{\mathbf{C}}\right)$ is the first invariant of the modified right Cauchy-Green deformation tensor, and $C_{10}$, $C_{20}$, $C_{30}$ and $K$ are material parameters, with K, the effective bulk modulus of the material calculated as:

$$K = \frac{2C_{10}\left(1+\nu\right)}{3\left(1-2\nu\right)}. \tag{2}$$

When the components are considered linear elastic, the Young modulus, $E$, is calculated by fitting the average stress-strain curve up to a strain of 10% deformation [15].

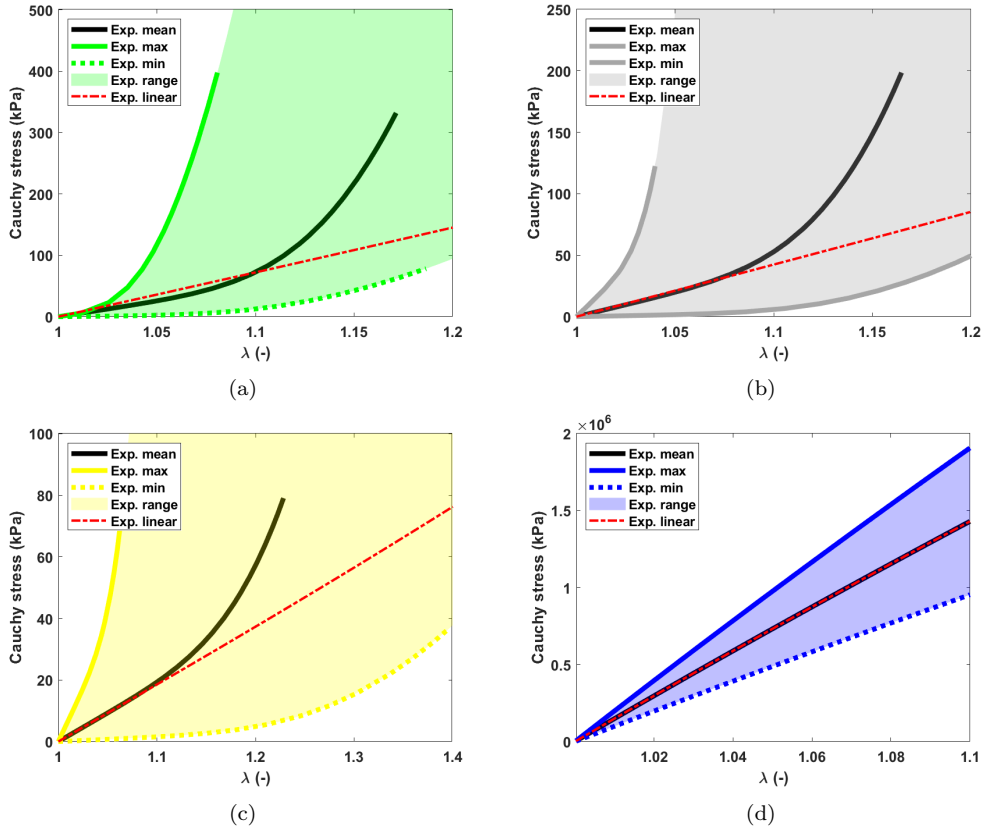


Figure 4: The stretch–stress curve of each tissue type with the corresponding averaged curve (black continuous line), maximum curve (colored continuous line), minimum curve (colored dashed line), linearised curve (red dashed and dotted line) and experimental range (colored area): (a) media; (b) loose matrix; (c) lipid core; and (d) calcification.

Figure 4 shows the stress-stretch curves of media [15], loose matrix, lipid core [15] and calcification [16] with the corresponding averaged, maximum, minimum, linearised curves and experimental range; while Table 1 shows the non-linear and linear elastic material properties of the media, loose matrix, lipid core, and calcification.

Table 1: Non-linear and linear elastic mechanical properties of media, loose matrix, lipid core, and calcification.

| | Non-linear elastic | | Linear elastic | |
|---|---|---|---|---|
| Tissue | Par. (kPa) | min/max/mean | Par. (kPa) | min/max/mean |
| Media | $C_{10}$ | 5.9e+0/7.0e+1/7.0e+1 | E | 8.9e+1/3.6e+3/7.3e+2 |
| | $C_{20}$ | 8.5e+1/2.1e+4/2.0e+2 | | |
| | $C_{30}$ | 6.4e+3/1.0e+6/1.9e+4 | | |
| | K | 1.2e+2/1.4e+3/1.4e+3 | | |
| Loose matrix | $C_{10}$ | 5.2e+0/2.6e+2/6.6e+1 | E | 2.9e+1/2.5e+3/4.3e+2 |
| | $C_{20}$ | – | | |
| | $C_{30}$ | 2.2e+3/4.7e+6/1.1e+4 | | |
| | K | 1.0e+2/5.2e+3/1.3e+3 | | |
| Lipid core | $C_{10}$ | 2.5e+0/1.1e+2/3.1e+1 | E | 1.3e+1/9.5e+2/1.9e+2 |
| | $C_{20}$ | – | | |
| | $C_{30}$ | 5.4e+1/2.2e+5/5.7e+2 | | |
| | K | 4.9e+1/2.3e+3/6.2e+2 | | |
| Calcium | E | – | E | 1.0e+7/2.0e+7/1.5e+7 |

To assess the impact of variability in mechanical properties, we considered 100 combinations of mechanical parameters within the range indicated in Table 1 for each component. These combinations were constrained to ensure that the stress-strain curve remained within the shaded area depicted in Figure 4. Table 2 provides a summary of the total simulations conducted for each group and case.

Table 2: Types of simulation performed for each group patient with the total number of patients, sections and simulations carried out.

| Simulation type | Patient group | N. patient | N. section | N. simulation |
|---|---|---|---|---|
| HV | G1 (unstable plaque) | 29 | 280 | 28000 |
| | G2 (stable plaque) | 26 | 250 | 25000 |
| HM | G1 (unstable plaque) | 29 | 280 | 280 |
| | G2 (stable plaque) | 26 | 250 | 250 |
| LV | G1 (unstable plaque) | 29 | 280 | 28000 |
| | G2 (stable plaque) | 26 | 250 | 25000 |
| LM | G1 (unstable plaque) | 29 | 280 | 280 |
| | G2 (stable plaque) | 26 | 250 | 250 |

Prior to conducting the simulations, a mesh sensitivity analysis was performed using triangular elements to determine the number of elements where the variation in simulation results (specifically, the peak PSS) was less than 5%. Additionally, a comparative analysis was carried out between results obtained using triangular elements (i.e., 3-node linear triangles) and quadrangular elements (i.e., 4-node bi-linear quadrangles), ensuring the discrepancy in peak PSS was less than 5%. Subsequently, the entire plaque model was meshed using 3-node linear triangles, yielding an average of approximately 100000 elements per model (Fig. 3b).

The model assumes no relative movement at the interface of atherosclerotic components. Both displacement and strain were assumed to be large. To prevent rigid body displacement, four points (highlighted as red/black points in Figure 3a) were fixed. To allow the vessel to expand in radial direction when pressure is applied, the four points were fixed in only one dimension, i.e., y-displacement is blocked for the two points on x-axis (red points of Figure 3a), while x-displacement is blocked for the two points on y-axis (black points of Figure 3a). In the FEM simulations, a pressure load (i.e., Neumann condition) was applied to the cross-section lumen (as depicted by the magenta curve in Figure 3a) in two steps. Initially, a ramp from 0 to diastolic pressure was applied, followed by a subsequent step in which the pressure was ramped from diastolic to systolic pressure. All FEM simulations were conducted using ABAQUS 2019 (Abaqus®). Additionally, the

URDFIL subroutine was utilized to extrapolate Cauchy principal stresses and logarithmic (real) principal strains at the centroid point for each model element under diastolic and systolic pressures.

*2.3. Geometric and stress markers of plaque vulnerability*

In clinical practice, the assessment of plaque vulnerability typically relies on geometric markers [18, 19, 20]. The analysis in this study considered the following geometric markers: luminal area (LA), area contoured by the external elastic membrane (EEM), plaque area (PLA), lipid core area (LCA), luminal stenosis (ST), vessel remodeling index (RI), plaque burden (PB), and percent lipid core (PLC). Specifically, LA represents the area bordered by the intima, while EEM denotes the area encircled by the external elastic lamina. PLA is calculated as EEM minus LA, and LCA represents the total area of the lipid core within the plaque. The determination of ST, RI, PB, and PLC was based on the formulas outlined by [18, 19]:

$$ST = 1 - \frac{LA}{LA_{ref}}, \tag{3}$$

$$RI = \frac{EEM - EEM_{ref}}{EEM_{ref}}, \tag{4}$$

$$PB = \frac{PLA}{EEM}, \tag{5}$$

$$PLC = \frac{LCA}{PLA}, \tag{6}$$

where $LA_{ref}$ is the reference luminal area calculated as LA in the proximal region, and $EEM_{ref}$ is the reference external elastic membrane area calculated as EEM area in the proximal region.

Throughout the analysis, vessel wall plaque structural stress (PSS) is described using maximum von MISES stress (pMISES) defined as

$$\text{pMISES} = \max_{i=1,N_e} \left(\text{MISES}_i^t\right), \tag{7}$$

where the subscript $i$ is the element number, $N_e$ the total number of elements in the model, and $t = \{dia, sys, dyn\}$ states for the specific time frame of interest. In particular, the dynamic pressure was defined as $P_{dyn} = P_{sys} - P_{dia}$, and the dynamic peak MISES, $\text{pMISES}^{dyn}$, was determined by:

$$\text{pMISES}^{dyn} = \max_{i=1,N_e} \left(\text{MISES}_i^{sys} - \text{MISES}_i^{dia}\right). \tag{8}$$

In addition to the time frame, we will distinguish between the different simulation types, namely: pMISES$^{dyn}$-X for pMISES$^{dyn}$ obtained with simulation X, with X={HM, HV, LM, LV}.

For the analysis of the results, since the calcification is the most rigid plaque component (i.e., with the highest Young modulus) and the plaque rupture never occurs in the calcification, the maximum von MISES stress was calculated excluding the elements of calcium and at the calcium interface from the entire cross-section area. This precaution allows to mitigate the error deriving from a sudden change in local mechanical properties of plaque tissue components, excluding zones characterised by a high gradient and excessive intensification of stress due to the calcification.

### *2.4. Machine Learning Classifier*

To assess the stratification performance of geometric markers and biomechanical variables, machine learning classifiers have been trained on 75% of the dataset and tested on the remaining 25% (a stratified partition was considered). Specifically, 12 decision tree classifiers were developed by considering single geometric markers (LA, EEM and PLA) presenting a significant difference in median values between the two patient populations and lower p-values (as detailed in the Results section 3.1), the combination of the three geometric markers, the combination of the diastolic, systolic and dynamic peak MISES (pMISES$^{dia}$, pMISES$^{sys}$ and pMISES$^{dyn}$) for the four different simulation types (HV, HM, LV, LM), and the combination of the diastolic, systolic and dynamic peak MISES and systolic and dynamic pressures for the four different simulation types (HV, HM, LV, LM). The models were developed in MATLAB R2022a (The MathWorks Inc). The results were evaluated in terms of area under the curve (AUC).

### *2.5. Statistical Analysis*

Data were assessed for normality using the Jarque-Bera test. Normally distributed continuous outcomes are presented as mean and were compared using unpaired t-test, while non-normal outcomes are presented as median and compared using the Wilcoxon rank sum test. All calculations were 2 tailed with p-value $<0.05$ considered statistically significant. Statistical analyses were performed in MATLAB R2022a, The MathWorks Inc.

accepted manuscript at https://doi.org/10.1016/j.cmpb.2024.108271

## 3. Results

### *3.1. Geometric marker results*

Geometric markers exhibited non-normal distribution, except for plaque burden. Statistical differences between the G1 and G2 patient groups were identified in the following parameters: LA, EEM, PLA, and PLC, although the discrepancy in PLC was minimal (see Table 3). Conversely, no significant differences were observed for LCA, ST, RI, and PB (refer to Table 3).

Table 3: Geometric markers for the G1 (unstable angina) and G2 (stable angina) group.

| Geometric marker | G1 group | G2 group | p-value |
|---|---|---|---|
| LA | 5.47 $mm^2$ | 4.70 $mm^2$ | $< 0.001$* |
| EEM | 19.87 $mm^2$ | 17.69 $mm^2$ | $< 0.001$* |
| PLA | 14.12 $mm^2$ | 12.14 $mm^2$ | $< 0.001$* |
| PLC | 0.029 | 0.032 | 0.046* |
| LCA | 0.42 $mm^2$ | 0.42 $mm^2$ | 0.73 |
| ST | $-0.20$ | $-0.21$ | 0.82 |
| RI | 0.53 | 0.57 | 0.89 |
| PB | 0.69 | 0.70 | 0.77 |

### *3.2. Peak MISES results*

Figure 5 shows the value of pMISES for the different types of simulation and different time frames.

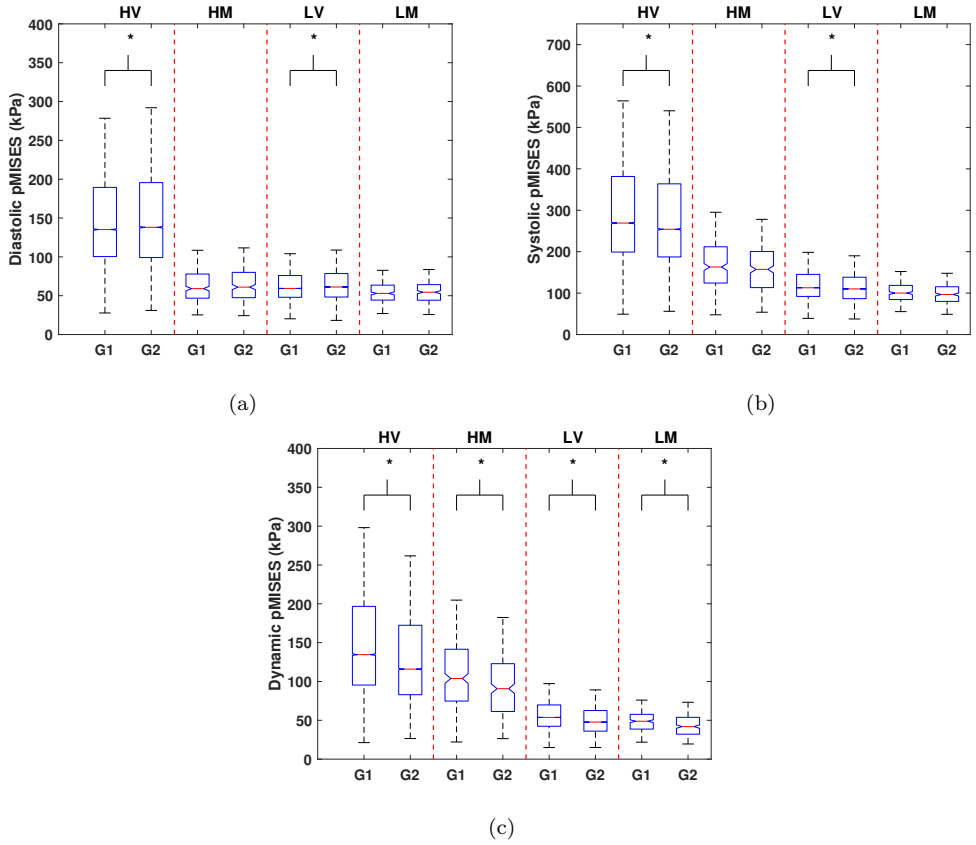


Figure 5: The boxplots of pMISES for the four types of simulations at three different time points: (a) diastolic, (b) systolic, and (c) dynamic condition. An asterisk (*) indicates a p-value <0.05; while HV indicates Hyper Variable simulations, HM Hyper Mean simulations, LV Linear Variable simulations, and LM Linear Mean simulations.

Statistical differences were observed for pMISES$^{dia}$ between G1 and G2 groups only for the hyper variable (HV) and linear variable (LV) model simulations (Fig. 5a). However, the average pMISES$^{dia}$ was notably larger and statistically different in simulations using a nonlinear material formulation with variable material properties (HV) in comparison to other simulations (detailed results not shown). Notably, outcomes from the HM model did not significantly differ from those using the linear variable material properties (LV). As expected, simulations utilizing variable material parameters show a larger variance compared to those using average material parameters. The coefficient of variation (CV) was calculated as 0.60 for HV, 0.48 for HM, 0.42 for LV, and 0.29 for LM.

Also, significant differences between G1 and G2 were observed only in the HV and LV simulations when considering pMISES$^{sys}$ stress (Fig. 5b). As in the case for pMISES$^{dia}$, the average pMISES$^{sys}$ was notably higher in simulations considering variable material properties, specifically 312 kPa for HV and 122 kPa for LV, compared to simulations considering average material parameters, which yielded values of 175 kPa for HM and 103 kPa for LM. Regarding result variability, the variance associated with pMISES$^{sys}$ was akin to that obtained for pMISES$^{dia}$, with CV measuring 0.61, 0.49, 0.42, and 0.28 for HV, HM, LV, and LM simulations.

Significant differences between G1 and G2 were observed in pMISES$^{dyn}$ across all four simulations (refer to Fig. 5c). Similar to the systolic and diastolic pressures, the average pMISES$^{dyn}$ was higher in the HV simulations (154 kPa) compared to the HM ones (109 kPa), and in the LV simulations (56 kPa) compared to the LM ones (47 kPa), with corresponding coefficients of variation (CV) of 0.67, 0.56, 0.47 and 0.35, respectively.

### *3.3. Machine Learning Classifier results*

Figure 6 shows the results of the developed decision tree classifiers on the test set. In particular, as shown in Figure 6a, the geometric markers (LA, EEM and PLA) exhibited a significant difference in median values between the two patient populations along with lower p-values (see Table 3) and their combination were associated with limited stratification performance (AUC [0.49 - 0.55]). Regarding the stratification efficacy of peak MISES stress, combinations of diastolic, systolic and dynamic peak MISES stresses in the HM, LM, and HV cases showed a modest enhancement in distinguishing between the two plaque populations compared to the geometric markers (AUC [0.56 - 0.60]). Notably, in the LV case, a substantial improvement was achieved, resulting in an AUC of 0.82 (Figure 6b). Finally, the inclusion of systolic and dynamic pressure to the peak MISES stresses further enhanced the predictive capability, yielding an AUC of 0.93 for HV case, an AUC of 0.91 for LV and HM cases, and slightly lower AUC of 0.86 for the LM case.

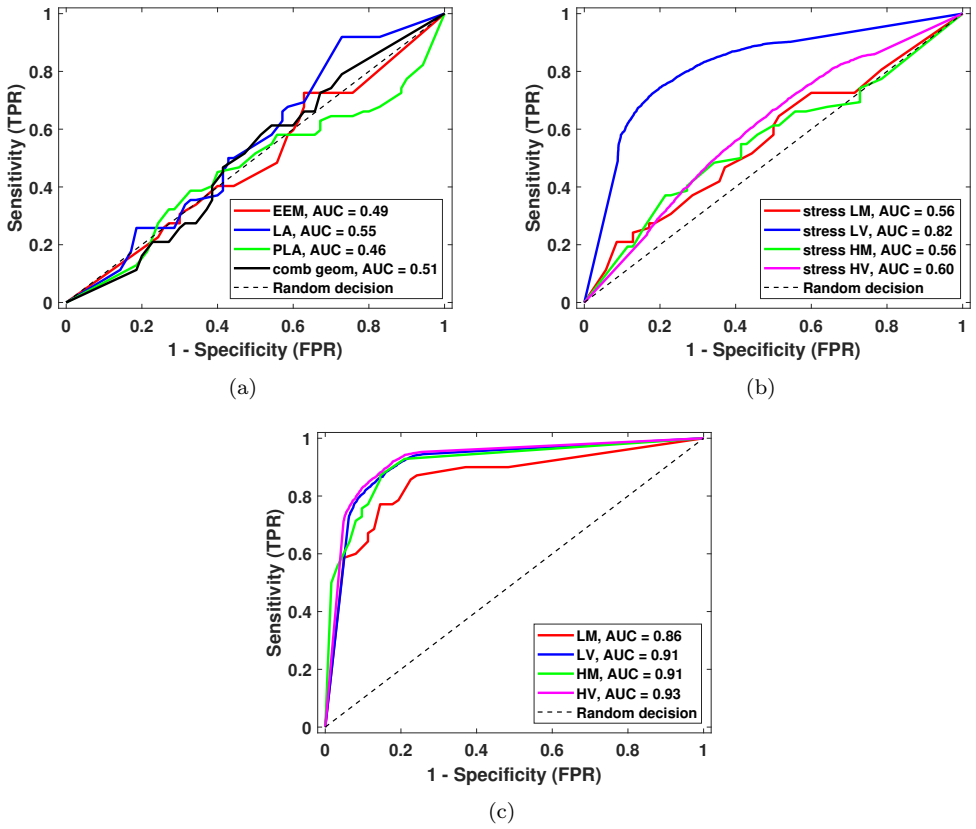


Figure 6: ROC of the decision tree classifiers: (a) single geometric markers (EEM, LA, PLA) and their combination; (b) combinations of diastolic, systolic, and dynamic peak MISES stresses for the HV, HM, LV, and LM cases; and (c) combinations of diastolic, systolic, and dynamic peak MISES stresses, in addition with systolic and dynamic pressure, for the HV, HM, LV, and LM cases.

## 4. Discussion

From the statistical analysis, the peak MISES calculated at the dynamic condition, pMISES$^{dyn}$, proved to be the most effective biomechanical marker in distinguishing between the two groups of patients. This underscores the importance of considering not only the conditions at the end of diastole or systole but also the entire pressure gradient ($\Delta P$) throughout the patient's cardiac cycle. This comprehensive approach might offer clinically relevant additional information for identifying unstable plaques and assessing the risk of plaque rupture in both patient groups. Moreover, pMISES demonstrated

better predictive capabilities than the combined geometric markers (i.e., LA, EEM and PLA ROC curves in Fig. 6a), a finding in line with the work by [13]. In particular, pMISES-LM showed superior predictive capabilities across all type of simulations. It stands as a robust predictor, being an independent parameter accessible for each plaque. It takes into account the geometric characteristics, composition, and distribution of different plaque components, along with the patient's blood pressure, while incorporating the uncertainty in the mechanical properties of the plaque components. It is worth noting that top, among all available patients, we selected only those where diastolic, systolic, and dynamic pressures were not different between the two groups. This selection aimed to eliminate bias arising from pressure differences. This emphasizes that the dissimilarity between the two populations evidenced by pMISES-LV simulations likely stems from differences in plaque geometries and composition. Additionally, it underscores the potential significance of the maximum pressure gradient during the cardiac cycle in influencing the mechanics of vulnerable (unstable) plaques, serving as an important clinical parameter for classifying a given plaque.

The ROC curves derived from simulations that incorporated the intrinsic variability of mechanical properties and linear elastic models showed the best performance. This outcome supports the common practice in the literature of using linear elastic models for plaque vulnerability classification [13, 17, 19, 21]. In addition, statistical analysis reveals that accounting for variability in mechanical properties enhances the capability to distinguish between the two populations. Hence, it is generally recommended to compute stress in the plaque while considering uncertainty in the mechanical properties. Interestingly, considering linear elastic material models for plaque components results in smaller average pMISES values compared to when using nonlinear hyperelastic models. However, our results demonstrate that this underestimation does not affect the marker's ability to differentiate between the two populations when material parameter uncertainty is considered.

An interesting result from our study, is the role of the patient's arterial pressure in the analysis. Despite the fact that no statistical differences exist between the diastolic, systolic and dynamic pressures, adding the systolic and dynamic pressures to the pMISES-LV at all three time frames further enhanced the predictive capability from an AUC=0.82 up to an AUC=0.91. Our results are comparable with other classifiers based on radiomic models [22] trained with similar size dataset (43 plaques) where an accuracy of

0.95 was achieved. In a more recent work [23] found 80% positive predictive values with a model based on a combination of structural and fluid-dynamic features on a 86 fibroatheromas from 67 patients. However, besides these studies demonstrate the potential of biomechanical markers for patient vulnerability classification, studies on larger populations and on more unbalanced groups are required to fully demonstrate this result.

Our study is not without limitations. For instance, while VH-IVUS was acquired pre-stenting, we lack information on the effects of plaque rupture, subsequent thrombosis, and healing before imaging. Therefore, a prospective validation of plaque structural stress (PSS), combined with other higher-risk features to predict major adverse cardiovascular events (MACEs) in a larger patient cohort, is essential [24, 25]. Moreover, the ability to estimate plaque stress partially depends on the resolution of VH-IVUS, and on the accuracy in identification of plaque components [24]. To date, VH-IVUS has been acknowledged as the imaging modality with most accurate identification of four plaque components, i.e., dense calcium, fibrous, fibrous-fatty and necrotic/lipid core; although a limited capability in detecting the necrotic/lipid core was reported. Other imaging modalities, such as optical coherence tomography (OCT) and coronary angioscopy, have different limitations. For example, OCT imaging is not suitable for plaques evaluation in coronaries with diameter >4 mm (penetration depth of OCT is 2 to 3 mm), and it cannot measure plaque area and volume. Also, it is necessary to continuously infuse contrast medium during probe pullback to reduce signal attenuation caused by red blood cells. Another OCT limitation is that estimation of lipid plaque component is challenging and quite subjective. On the other hand, coronary angioscopy is not able to identify all plaques within vessel wall, since the visualized area of this imaging method is limited [28]. Considering all the above, VH-IVUS was the best imaging modality for the purpose of the present study, since it is able to accurately identify both plaque size and composition with sufficient resolution for FEM analysis. Moreover, there are prospective data correlating VH-defined plaque features to clinical events [13]. In addition, our patient cohort is quite balanced in terms of vulnerable and non-vulnerable cases, a scenario quite different from what is normally found in clinical practice where vulnerable cases are found in a significant lower number with respect to non-vulnerable patients. Future work will consider classification of more realistic cohort of patients.

Furthermore, in our study we only considered geometric and stress markers, such as LA, EEM, PLA, stenosis, remodeling index, plaque burden and

peak von MISES stress (pMISES), since clinically annotated conventional plaque vulnerability markers (as napkin-ring sign, spotty calcification and low attenuation plaque) were not available, although their recognized importance. Including these markers, as well as other image-derived features could help in improving coronary vulnerable plaque detection and patient stratification. Towards this direction, an ongoing study from our group is aimed at the development of a combined radiomic-biomechanical predictive model, based on a coronary computed tomography angiography (CCTA) dataset. Also, the effect of biochemical transport in the progression of a vulnerable plaque was not considered in this work. The integration of a transport model of metabolites (e.g., low-density lipoprotein) in the current workflow might enhance the classification ability between vulnerable and non-vulnerable plaques.

As our FEM simulations were 2D, the proposed model only considered the plaque structural stress deriving from the systolic/diastolic pressures and the effect of blood flow was neglected. Nevertheless, given that PSS within plaques is significantly greater than wall shear stress due to blood flow, it is plausible to assume that shear stress plays a limited role in overall plaque stress [26]. However, in future, wall-shear stress based descriptors can be derived from computational fluid dynamics (CFD) simulations and integrated in a more comprehensive predictive model of plaque vulnerability [29]. Additionally, we analysed only 10 sections per patient; accounting for more sections could enhance analysis accuracy and the differentiation between the two atherosclerotic plaque populations. Lastly, the coronary geometries were obtained during diastole, under pressure. In order to establish the zero-pressure condition for computational simulation, a more reliable and direct methodology, based on inverse elastostatics [27], could be employed to identify the zero-pressure geometry, allowing for a more accurate risk assessment.

## 5. Conclusion

In summary, our results emphasize that peak MISES serves as a strong predictor, as it independently considers stress in all directions and incorporates total geometric features of atherosclerotic plaques. The combination of diastolic, systolic and dynamic pMISES with patient's systolic and dynamic pressures might play a significant role as mechanical biomarkers for classification of vulnerable plaques. Notably, our study illustrates that distinguishing between the two populations of atherosclerotic plaques is more reliant on stress state than on plaque geometric features when the uncertainty in the

material properties is considered. Last but not least, biomechanical markers based on peak plaque stress could be combined with radiomic features of the plaque to obtained more robust classifiers of plaque vulnerability.

## Acknowledgments

*Statements of ethical approval*

None.

*Funding*

This project received funding from: i) the "Ministero dell'Istruzione, dell'Università e della Ricerca (MIUR)", "Fondo integrativo speciale per la ricerca" (FISR) under the CECOMES ("CEntro di studi sperimentali e COmputazionali per la ModElliStica applicata alla chirurgia") project aimed at the development of models representing the situation and characteristics of the specific patient, and aimed at the optimal planning of interventions and decision making (grant agreement N. FISR2019_03221); and ii) Fondazione Regionale per la Ricerca Biomedica (Regione Lombardia), project ID 3432721. The VIVA study was supported by British Heart Foundation grants PG/08/008 and FS/10/025/28196 and by the National Institute for Health Research Cambridge Biomedical Research Centre.

*Competing interests*

Zhongzhao Teng is the Chief Scientist of Tenoke Ltd., UK and Nanjing Jingsan Medical Science & Technology Ltd., China. The other authors declare that they have no conflicts of interest that could have appeared to influence the work reported in this paper.

## References

[1] J. F. Bentzon, F. Otsuka, R. Virmani, E. Falk, Mechanisms of plaque formation and rupture, Circulation research 114 (12) (2014) 1852–1866.

[2] D. Opincariu, T. Benedek, M. Chițu, N. Rațț, I. Benedek, From ct to artificial intelligence for complex assessment of plaque-associated risk, The International Journal of Cardiovascular Imaging 36 (12) (2020) 2403–2427.

[3] R. Virmani, F. D. Kolodgie, A. P. Burke, A. Farb, S. M. Schwartz, Lessons from sudden coronary death: a comprehensive morphological classification scheme for atherosclerotic lesions., Arteriosclerosis, thrombosis, and vascular biology 20 (2000) 1262–75.

[4] A. Nair, B. D. Kuban, E. M. Tuzcu, P. Schoenhagen, S. E. Nissen, D. G. Vince, Coronary plaque classification with intravascular ultrasound radiofrequency data analysis., Circulation 106 (2002) 2200–6.

[5] D. R. Obaid, P. A. Calvert, D. Gopalan, R. A. Parker, S. P. Hoole, N. E. J. West, M. Goddard, J. H. F. Rudd, M. R. Bennett, Atherosclerotic plaque composition and classification identified by coronary computed tomography: assessment of computed tomography-generated plaque maps compared with virtual histology intravascular ultrasound and histology., Circulation. Cardiovascular imaging 6 (2013) 655–64.

[6] P. A. Calvert, D. R. Obaid, M. O'Sullivan, L. M. Shapiro, D. McNab, C. G. Densem, P. M. Schofield, D. Braganza, S. C. Clarke, K. K. Ray, N. E. J. West, M. R. Bennett, Association between ivus findings and adverse outcomes in patients with coronary artery disease: the viva (vh-ivus in vulnerable atherosclerosis) study., JACC. Cardiovascular imaging 4 (2011) 894–901.

[7] G. W. Stone, A. Maehara, A. J. Lansky, B. de Bruyne, E. Cristea, G. S. Mintz, R. Mehran, J. McPherson, N. Farhat, S. P. Marso, H. Parise, B. Templin, R. White, Z. Zhang, P. W. Serruys, A prospective natural-history study of coronary atherosclerosis., The New England journal of medicine 364 (2011) 226–35.

[8] K. Y. Lee, K. Chang, Understanding vulnerable plaques: current status and future directions, Korean Circulation Journal 49 (12) (2019) 1115–1122.

[9] C. Stefanadis, C.-K. Antoniou, D. Tsiachris, P. Pietri, Coronary atherosclerotic vulnerable plaque: current perspectives, Journal of the American Heart Association 6 (3) (2017) e005543.

[10] M. J. Bom, D. J. Van Der Heijden, E. Kedhi, J. Van Der Heyden, M. Meuwissen, P. Knaapen, S. A. Timmer, N. Van Royen, Early detection and treatment of the vulnerable coronary plaque: can we prevent

acute coronary syndromes?, Circulation: cardiovascular imaging 10 (5) (2017) e005973.

[11] Y. Vengrenyuk, S. Carlier, S. Xanthos, L. Cardoso, P. Ganatos, R. Virmani, S. Einav, L. Gilchrist, S. Weinbaum, A hypothesis for vulnerable plaque rupture due to stress-induced debonding around cellular microcalcifications in thin fibrous caps., Proceedings of the National Academy of Sciences of the United States of America 103 (2006) 14678–83.

[12] H. Huang, R. Virmani, H. Younis, A. P. Burke, R. D. Kamm, R. T. Lee, The impact of calcification on the biomechanical stability of atherosclerotic plaques., Circulation 103 (2001) 1051–6.

[13] Z. Teng, A. J. Brown, P. A. Calvert, R. A. Parker, D. R. Obaid, Y. Huang, S. P. Hoole, N. E. J. West, J. H. Gillard, M. R. Bennett, Coronary plaque structural stress is associated with plaque composition and subtype and higher in acute coronary syndrome: the beacon i (biomechanical evaluation of atheromatous coronary arteries) study., Circulation. Cardiovascular imaging 7 (2014) 461–70.

[14] Y. Huang, Z. Teng, U. Sadat, S. Hilborne, V. E. Young, M. J. Graves, J. H. Gillard, Non-uniform shrinkage for obtaining computational start shape for in-vivo mri-based plaque vulnerability assessment., Journal of biomechanics 44 (2011) 2316–9.

[15] Z. Teng, Y. Zhang, Y. Huang, J. Feng, J. Yuan, Q. Lu, M. P. F. Sutcliffe, A. J. Brown, Z. Jing, J. H. Gillard, Material properties of components in human carotid atherosclerotic plaques: a uniaxial extension study., Acta biomaterialia 10 (2014) 5055–5063.

[16] D. M. Ebenstein, D. Coughlin, J. Chapman, C. Li, L. A. Pruitt, Nanomechanical properties of calcification, fibrous tissue, and hematoma from atherosclerotic plaques., Journal of biomedical materials research. Part A 91 (2009) 1028–37.

[17] A. Milzi, E. D. Lemma, R. Dettori, K. Burgmaier, N. Marx, S. Reith, M. Burgmaier, Coronary plaque composition influences biomechanical stress and predicts plaque rupture in a morpho-mechanic oct analysis., eLife 10 (May 2021).

[18] A. M. Varnava, P. G. Mills, M. J. Davies, Relationship between coronary artery remodeling and plaque vulnerability., Circulation 105 (2002) 939–43.

[19] S. Inaba, G. S. Mintz, N. Z. Farhat, J. Fajadet, D. Dudek, A. Marzocchi, B. Templin, G. Weisz, K. Xu, B. de Bruyne, P. W. Serruys, G. W. Stone, A. Maehara, Impact of positive and negative lesion site remodeling on clinical outcomes: insights from prospect., JACC. Cardiovascular imaging 7 (2014) 70–8.

[20] E. Conte, A. Annoni, G. Pontone, S. Mushtaq, M. Guglielmo, A. Baggiano, V. Volpato, C. Agalbato, A. Bonomi, F. Veglia, A. Formenti, C. Fiorentini, A. L. Bartorelli, M. Pepi, D. Andreini, Evaluation of coronary plaque characteristics with coronary computed tomography angiography in patients with non-obstructive coronary artery disease: a long-term follow-up study, European Heart Journal - Cardiovascular Imaging 18 (10) (2017) 1170–1178.

[21] S. Yang, B.-K. Koo, M. Hoshino, J. M. Lee, T. Murai, J. Park, J. Zhang, D. Hwang, E.-S. Shin, J.-H. Doh, C.-W. Nam, J. Wang, S. Chen, N. Tanaka, H. Matsuo, T. Akasaka, G. Choi, K. Petersen, H.-J. Chang, T. Kakuta, J. Narula, Ct angiographic and plaque predictors of functionally significant coronary disease and outcome using machine learning, JACC: Cardiovascular Imaging 14 (3) (2021) 629–641.

[22] Q. Chen, T. Pan, X. Yin, H. Xu, X. Gao, X. Tao, L. Zhou, G. Xie, X. Kong, X. Huang, et al., Ct texture analysis of vulnerable plaques on optical coherence tomography, European Journal of Radiology 136 (2021) 109551.

[23] S. Z. Gu, M. E. Ahmed, Y. Huang, D. Hakim, C. Maynard, N. V. Cefalo, A. U. Coskun, C. Costopoulos, A. Maehara, G. W. Stone, et al., Comprehensive biomechanical and anatomical atherosclerotic plaque metrics predict major adverse cardiovascular events: A new tool for clinical decision making, Atherosclerosis 390 (2024) 117449.

[24] C. Costopoulos, A. Maehara, Y. Huang, A. J. Brown, J. H. Gillard, Z. Teng, G. W. Stone, M. R. Bennett, Heterogeneity of plaque structural stress is increased in plaques leading to mace: insights from the prospect study, Cardiovascular Imaging 13 (5) (2020) 1206–1218.

[25] A. J. Brown, Z. Teng, P. A. Calvert, N. K. Rajani, O. Hennessy, N. Nerlekar, D. R. Obaid, C. Costopoulos, Y. Huang, S. P. Hoole, et al., Plaque structural stress estimations improve prediction of future major adverse cardiovascular events after intracoronary imaging, Circulation: Cardiovascular Imaging 9 (6) (2016) e004172.

[26] U. Sadat, Z. Teng, J. H. Gillard, Biomechanical structural stresses of atherosclerotic plaques., Expert review of cardiovascular therapy 8 (2010) 1469–81.

[27] M. Peirlinck, M. De Beule, P. Segers, N. Rebelo, A modular inverse elastostatics approach to resolve the pressure-induced stress state for in vivo imaging based cardiovascular modeling., Journal of the mechanical behavior of biomedical materials 85 (2018) 124–133.

[28] S. Kitahara, Y. Kataoka, H. Sugane, F. Otsuka, Y. Asaumi, T .Noguchi, S. Yasuda, In vivo imaging of vulnerable plaque with intravascular modalities: its advantages and limitations., Cardiovascular Diagnosis and Therapy 10(5) (2020) 1461–1479.

[29] G. De Nisco, C. Chiastra, E. M. J. Hartman, A. Hoogendoorn, J. Daemen, K. Calò, D. Gallo, U. Morbiducci, J. J. Wentzel, Comparison of Swine and Human Computational Hemodynamics Models for the Study of Coronary Atherosclerosis., Frontiers in bioengineering and biotechnology 9 (2021) 1–13.